Journal of Volcanology and Geothermal Research 184 (2009) 367–380

Contents lists available at ScienceDirect

Journal of Volcanology and Geothermal Research

journal homepage: www.elsevier.com/locate/jvolgeores

The 2005 eruption of Kliuchevskoi volcano: Chronology and processes derived from ASTER spaceborne and field-based data

Shellie Rose *, Michael Ramsey

Department of Geology and Planetary Science, University of Pittsburgh, Pittsburgh, PA, 15260, USA

ARTICLE INFO

Article history:
Received 15 October 2008
Accepted 4 May 2009
Available online 7 May 2009

Keywords:
ASTER
Kliuchevskoi
Kamchatka
temperature
remote sensing

ABSTRACT

Kliuchevskoi volcano, located on the Kamchatka peninsula of eastern Russia, is one of the largest and most active volcanoes in the world. Its location and diversity of eruption styles make satellite-based monitoring and characterization of its eruptive activity essential. In 2005, the Kamchatka Volcano Emergency Response Team (KVERT) first reported that seismic activity of Kliuchevskoi increased above background levels on 12 January (Kamchatka Volcanic Eruption Response Team (KVERT) Report, 2005. Kliuchevskoi Volcano, 14 January through 13 May 2005. (http://www.avo.alaska.edu/activity/avoreport.php?view=kam info&id=&month=January&year=2005). Cited January 2007). By 15 January Kliuchevskoi entered an explosive–effusive phase, which lasted for five months and produced basaltic lava flows, lahar deposits, and phreatic explosions along its northwestern flank. We present a comparison between field observations and multispectral satellite image data acquired by the Advanced Spaceborne Thermal Emission and Reflection Radiometer (ASTER) instrument in order to characterize the eruptive behavior. The ASTER instrument was targeted in an automated urgent request mode throughout the eruption timeline in order to collect data at the highest observation frequency possible. Brightness temperatures were calculated in all three ASTER wavelength regions during lava flow emplacement. The maximum lava flow brightness temperatures, calculated from the 15 m/pixel visible near infrared (VNIR) data, were in excess of 800 °C. The shortwave infrared (SWIR) data were radiometrically and geometrically corrected, normalized to the same gain settings, and used to estimate an eruptive volume of 2.35×10^{-2} km^3 at the summit. These data were also used to better constrain errors arising in the thermal infrared (TIR) data due to sub-pixel thermal heterogeneities. Based on all the ASTER data, the eruption was separated into three phases: an initial explosive phase (20 January–31 January), an explosive–effusive phase (1 February–8 March), and a subsequent cooling phase. Decorrelation stretch (DCS) images of the TIR data also suggested the presence of silicate ash, SO_2, and water vapor plumes that extended up to 300 km from the summit. The ASTER rapid-response program provided important multispectral, moderate spatial resolution information that was used to detect and monitor the eruptive activity of this remote volcano which can be applied to other eruptions worldwide.

1. Introduction

The Kamchatka Peninsula of eastern Russia is one of the most volcanically active regions in the world and eruptions there can pose hazards such as lahars, pyroclastic flows, earthquakes, and ashfall to the sparse population centers. Larger ash-producing eruptions can also impact the greater northern Pacific region by way of interaction with the approximately 200 aircraft and 20,000 people overflying the region daily (Miller and Casadevall, 2000). The interaction between micron to submicron-sized glassy ash shards and aircraft engines can cause catastrophic consequences such as severe abrasion to external surface components and welding of ash to mechanical elements, ultimately leading to engine failure (Casadevall, 1993; Self and Walker, 1994; Casadevall, 1994; Przedpelski and Casadevall, 1994; Searcy et al., 1998; Miller and Casadevall, 2000; Pieri et al., 2002). Additionally, eruptions occurring in this region have the potential to transition in behavior and intensity over a short period of time, as observed through edifice collapse, explosive eruptions, and lava dome formation of Bezymianny and Shiveluch volcanoes (Eichelberger and Eichelberger, 2008). For these reasons, it is critical to monitor and characterize eruptive activity of this region in order to better recognize the precursors of future behavior, and thus minimize risks locally and abroad.

Kliuchevskoi volcano (56° 11′N, 160° 47′E), located at the intersection of the Aleutian and Kuril–Kamchatka volcanic arcs, is the highest (4835 m) and one of the most restless of Kamchatka's 29 active volcanoes (Fig. 1). It produces and average of 6.0×10^7 tons of material per year and contains over 250 km^3 of high-magnesian to high-aluminous basaltic-andesite material (Fedotov et al., 1987; Fedotov and Masurenkov, 1991; Ozerov et al., 1997). The Kliuchevskoi eruptive dynamics have been separated into three distinct styles: flank, summit,

* Corresponding author. Tel.: +1 412 624 8780.
E-mail address: srr13@pitt.edu (S. Rose).

0377-0273/$ – see front matter © 2009 Elsevier B.V. All rights reserved.
doi:10.1016/j.jvolgeores.2009.05.001

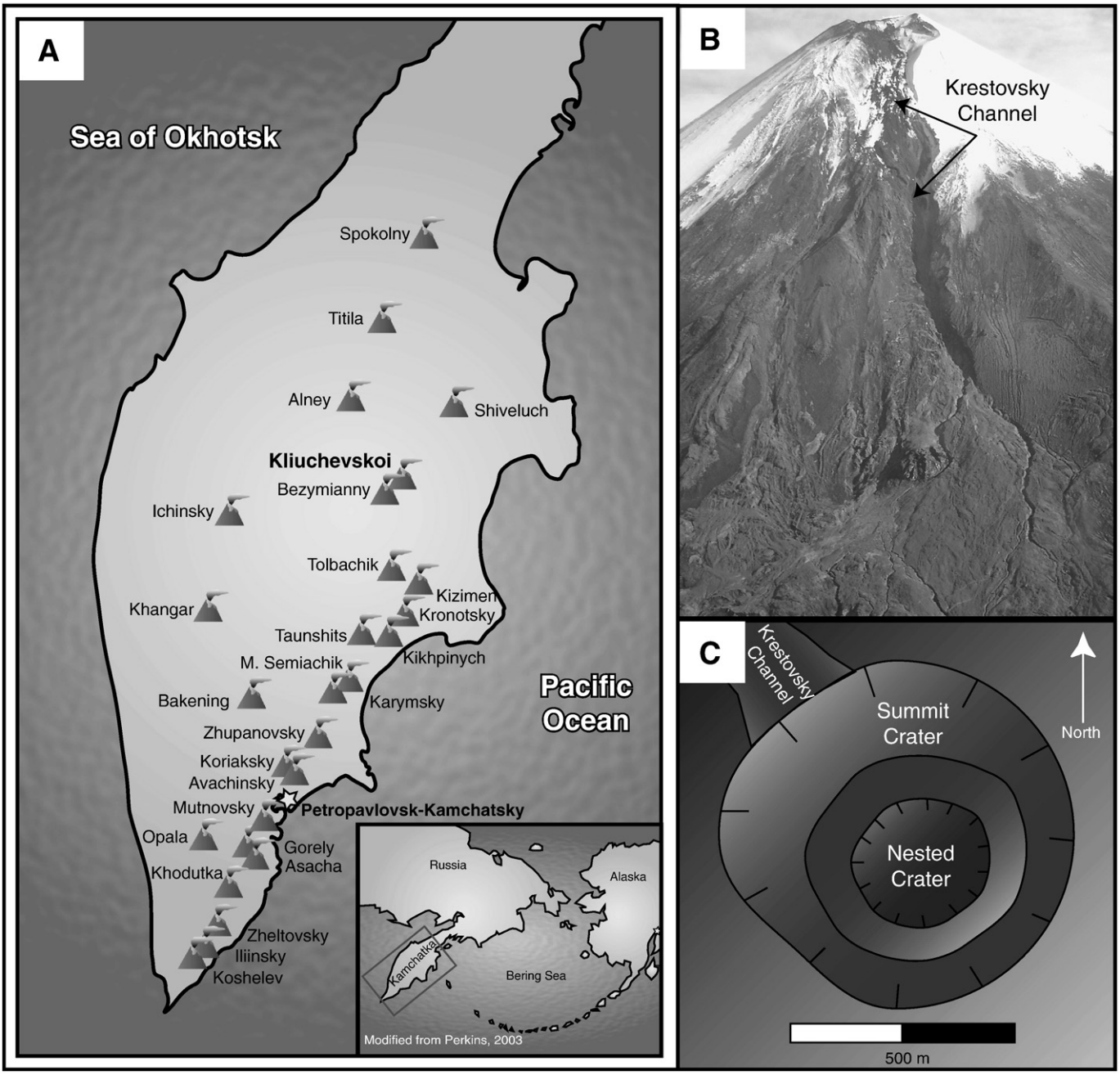

Fig. 1. (A) Location map of the Kamchatka Peninsula of far eastern Russia including the locations of the most active volcanoes in the region. Kliuchevskoi is highlighted in red. (B) A field photograph taken in August of 2005, approximately 3 months following the last data acquisition presented here. The view is looking toward the northwestern flank at the Krestovsky Channel. (C) A sketch map showing locations and extent of primary Kliuchevskoi features such as the summit crater, nested summit crater, and Krestovsky Channel. The dashed line indicates maximum extent of lava flows throughout the eruption and initiation point of the lahars.

and paroxysmal eruptions, with each having occurred in the last 21 years (Fedotov and Masurenkov, 1991).

Sixteen historical flank eruptions have been documented from as early as 1907 (Smithsonian GVP, 2008) although a significant change in eruptive behavior, from summit to flank activity, has been noted following the 1932 eruption (Fedotov and Masurenkov, 1991). These types of eruptions typically start with the formation of radial linear fissures that produce explosive craters and explosive/effusive cinder cones at higher and lower elevations, respectively. The low elevation cinder cones have produced numerous blocky lava flows as large as 0.5 km^3 with eruption duration ranging from 5 days to 13 months (Fedotov and Masurenkov, 1991). The last recent flank eruption occurred during the 1984–1987 phase of activity with the opening of a fissure along the southeastern flank (3800 to 3400 m ASL) and the eruption of a lava flow down slope (Smithsonian GVP, 2008; Fedotov and Masurenkov, 1991). From that time, eruption activity has been constrained to the summit crater and lava flows emplaced from the summit (Smithsonian GVP, 2008).

Summit eruptions at Kliuchevskoi have been documented since 1697 and are characteristically Strombolian to Plinian in style, longer in duration than the flank eruptions, and occur approximately every 25 years (Gushchenko, 1979; Fedotov and Masurenkov, 1991). However, in the last century, summit eruptions have increased significantly with one eruption occurring every 1–2 years (Smithsonian GVP, 2008). This suggests that the volcano may have entered a new phase of open-conduit-heightened activity. Typically, summit eruptions at Kliuchevskoi have

started as increased fumarolic activity and phreatic explosions within the central crater that are caused by rising magma interacting with melt water from the permanent snow/ice cover, and subsequent formation of a summit crater lava lake. Increased thermal activity near the summit, including the ejection of volcanic bombs, effusion of blocky lava flows, and hot avalanches have commonly followed and produced lahars tens of kilometers down the flanks into the nearby Kruten'kaya River (Fedotov and Masurenkov, 1991; Smithsonian GVP, 2008). Over the past 300 years, these types of eruptions have resulted in cyclical changes in the summit morphology (Fedotov et al., 1987), with lava infilling of the crater producing the overall conical shape, and paroxysmal eruptions destroying the summit edifice (Fedotov and Masurenkov, 1991).

The first historic paroxysmal summit eruption occurred in 1738 and the most recent in 1994. Descriptions of the 1738 eruption document a week of explosive activity that included incandescent, "audible" lava flows (most likely the result of interaction with snow/ice), notable seismic activity (trembling ground), and sizeable ash plumes (Krasheninnikov, 1949). These ash plumes were reported to have migrated toward the sea and produced little to no fallout locally, implying that the plume had reached the stratosphere (>12 km at the latitude of Kliuchevskoi) where rapid transport occurred. Similarly, in 1994 Kliuchevskoi entered its largest eruptive phase in over 40 years (Miller et al., 1994). On 8 September this eruption initiated with minor explosive activity within the summit crater producing low-level ash clouds (<9 km ASL), below the cruising altitude of aircraft. However, by 30 September the eruption intensified to a paroxysmal state with large convecting columns producing pyroclastic flows, as well as lahars and lava flows ($\sim 3.0 \times 10^7$ m^3) (Smithsonian GVP, 2008). The largest explosive eruptions (VEI = 3) produced a significant ash column (Fig. 2) containing $\sim 5.0 \times 10^7$ m^3 of material that reached 18 km ASL and traveled approximately 1000 km southeast into the North Pacific air traffic routes (Miller et al., 1994). This intense explosive stage of the eruption continued for roughly 36 h and eventually subsided by 2 October. From that time, Kliuchevskoi has remained relatively active, producing smaller explosive eruptions (VEI = 1–2) and effusive activity on a 1–2 year time scale (Smithsonian GVP, 2008).

2. Volcano monitoring of the North Pacific

In 1993, a collaborative effort between scientists from the Alaska Volcano Observatory (AVO), the Russian Academy of Sciences Institute of Volcanic Geology and Geochemistry (IVGG), the Kamchatkan Experimental and Methodical Seismological Department (KEMSD), established the Kamchatkan Volcanic Eruption Response Team (KVERT) (Kirianov et al., 2002). This group was created from the existing Russian institutions and designed for rapid detection and response to volcanic activity on the Kamchatka Peninsula. The main function of KVERT is to provide eruption notices and status reports to local and international authorities in order to reduce associated risks to aircraft within the vicinity of drifting volcanic ash plumes (Heiken et al., 1992).

Presently, the principal methods for monitoring volcanic unrest in this region include seismic stations, ground-based visual observations, and low spatial resolution (e.g., 1 km/pixel and larger) and high temporal resolution (e.g., 1–6 h) satellite data. As of 2007, 33 remote seismic stations have been deployed throughout the most active volcanic areas on Kamchatka (Chebrov, 2008). In order to augment human observations and verify eruptive activity, a web-based video camera system focused on Kliuchevskoi was installed in the town of Klyuchi in 2000. Periodic overflights are also conducted to provide visual observations. These real time descriptions and images are compared to seismic data in order to scale visible plume heights to seismic energy (Roach et al., 2004). During periods of bad weather where visual observations are impossible, plume heights can therefore be estimated based solely on the seismic activity. As the technology has increased in sophistication visible and thermal infrared satellite-based instruments have been used to detect and model plume height, compositions, density, and temperature during an eruption (Rothery, 1989; Realmuto et al., 1994, 1997; Searcy et al., 1998; Dehn et al., 2002; Ramsey and Dehn, 2004; Vaughan et al., 2005). Presently, the instruments used to monitor volcanic activity of Kliuchevskoi and other active volcanoes of the North Pacific region include the Geostationary Operational Environmental Satellites (GOES), the Advanced Very High Resolution Radiometer (AVHRR), and the Moderate Resolution Imaging Spectroradiometer (MODIS), which

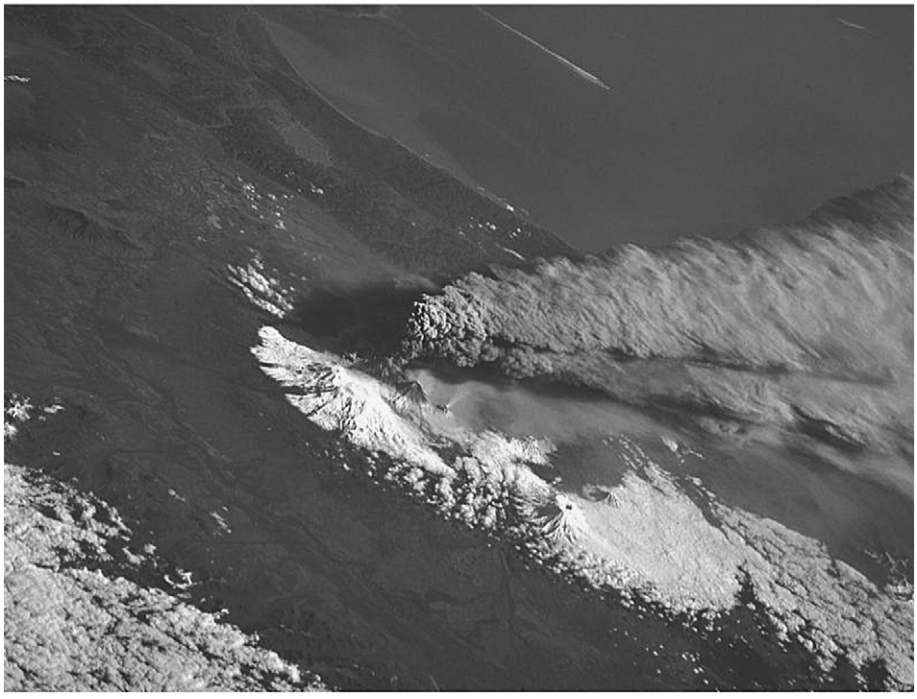

Fig. 2. The 1994 eruption of Kliuchevskoi volcano observed from the space shuttle Endeavor. During this paroxysm the ash plume reached an altitude of 18 km ASL as it migrated southeastward towards the North Pacific Ocean.

acquire data every 15 min, 4–6 h, and 3–4 h, respectively. Although ideal for detection and monitoring of hourly changes at an active volcano, high temporal/low spatial resolution data provided by these sensors can commonly miss smaller-scale observations. Thermally-anomalous pixels are only detectable if the erupted material is either very hot and/or covers a large percentage of the pixel. Furthermore, the inability to determine parameters such as composition, surface texture, and heat flux of small lava flows/fumaroles in sufficient detail makes these sensors non-ideal for small-scale mapping and monitoring. In order to extract and document detailed eruptive processes and behavior of Kliuchevskoi volcano, currently unobtainable by these sensors, we intend to utilize the high-spatial resolution ASTER instrument.

The goal of this investigation is to characterize a rarely documented eruption of a remote, yet hazardous volcano by using remote sensing data from a broad spectral range and spatial resolutions under 100 m/pixel, and extract maximum integrated brightness temperatures to identify correlations between color codes of concern and associated eruptive behaviors. This analysis will document the assessment of the maximum integrated brightness temperature of the erupted products, the spatial extent of these products, the errors involved, and the overall usefulness of these data for extraction of the ongoing volcanological processes occurring during the 2005 eruption of Kliuchevskoi volcano.

3. 2005 Kliuchevskoi eruption observations and data

3.1. KVERT observations

During the 2005 eruption, KVERT disseminated multiple information releases, which summarized the most recent observations (Table 1). On 12 January 2005, KVERT reported increased seismic and thermal activity at Kliuchevskoi. In addition, a weak gas–steam plume was observed emanating from the summit. Two days later, KVERT raised the color code from green to yellow and eventually, from yellow to orange on 16 January due to the increasing seismic activity as well as the incandescence observed above the crater. By the end of January, gas–water vapor plumes rose between 800 and 1500 m above the crater and Strombolian activity had initiated. Volcanic bombs were also observed being ejected 50–300 m above the crater on the evenings of 20–23 January and again on 27 January.

Throughout February and March, the eruption remained dynamic, with seismic activity well above background level. Plumes containing acid gases, water vapor, steam, and ash in varying amounts, hereafter called 'plumes', were more energetic, rising to more than 3000 m above the summit and occasionally produced ash fall that was observed on the flank of nearby Ushkovsky volcano (northwestern portion of the Kliuchevskaya group), and in the towns of Klyuchi and Kozyrevsk. In early February, lava was first observed in the Krestovsky channel on the northwestern flank of Kliuchevskoi (Fig. 1). The interaction of this flow with the summit glaciers and snow cover produced phreatic explosions and subsequent lahars. However, mobility of the flow by mid-March was limited due to cooling and continued lava effusion from the summit produced a second flow. During this two-month period, Strombolian explosions became more vigorous, with explosions observed as high as 1000 m above the crater. The hazard level color code was raised from orange to red on 24 March and returned to orange four days later as seismic activity and volcanic tremor decreased.

The eruption activity began to lessen in April and throughout May. Both seismic activity and frequency of visual observations decreased, and the color code was lowered to yellow by 15 April. The lava flow was no longer advancing and although production of plumes continued, they rarely reached 1000 m above the summit Strombolian activity ceased and seismic activity reached background levels by 29 April. Although seismic activity varied over the next few months, no significant volcanic changes were noted after 16 May and the hazard level color code was eventually lowered to green on 12 August, approximately one week prior to our field investigation. The ASTER data presented here span January through March, the most vigorous phase of the 2005 eruption.

3.2. ASTER instrument and data

The ASTER sensor was launched in December 1999 as one of five instruments on the Terra satellite, part of NASA's Earth Observing System (EOS). Terra follows a sun-synchronous nearly polar orbit with an equator crossing time of ~10:30 am/pm. The ASTER instrument has a 60 km swath width, which allows any point on the surface to be imaged at least once every 16 days. At higher latitudes and with the capability of the sensor to point in the cross-track direction, this revisit time can be reduced to 1–5 days (Yamaguchi et al., 1998, Ramsey and Dehn, 2004). ASTER contains 14 spectral bands including three in the VNIR region (0.5 to 1.0 μm) with 15 m spatial resolution, six in the shortwave infrared (SWIR) region (1.0 to 2.5 μm) with 30 m spatial resolution, and five within the thermal infrared (TIR) region (8 to 12 μm) with 90 m spatial resolution (Kahle et al., 1991). In conjunction with the nominal nadir viewing, an additional backward-looking telescope with the same spectral and spatial resolution as VNIR band 3 (0.807 μm), provides along-track stereographic imaging capability in order to produce digital elevation models (DEMs).

From its initial calibrated data release in March of 2000, ASTER has proven effective for the detection and monitoring of volcanic eruptions and their associated products. Ramsey and Dehn (2004) and Pieri and Abrams (2004) outline five benefits of ASTER data as compared to other sensors for volcanic monitoring. These include the ability to acquire nighttime TIR and SWIR data, variable spatial resolution for the different wavelength regions, image acquisition up to 85° latitude,

Table 1
Summary of KVERT information releases throughout the 2005 eruption (KVERT, 2005). ASTER acquisitions dates are listed and the associated observations were released within several days. The level of concern color code is included to show relationships between the eruption characteristics and hazard level. EQ = earthquakes; T = volcanic tremor.

Acquisition date	Color code	Seismicity	Plumes	Plume expanse	Explosions	Lava flows	Lahars	Other
15-Jan	Yellow	EQ (MI>1.25) T (3.2×10^{-6})	Gas–steam					Crater luminescence
22-Jan	Orange	EQ (MI 1.2–2.5) T (12.2×10^{-6})	Gas–steam ash	>10.6 km	Strombolian			
7-Feb	Orange	EQ (MI 1.4–2.4) T (12.6×10^{-6})	Gas–steam ash	4.1 km	Strombolian	Effusion	Lahars	Summit crater cinder cone forms. Ash fallout on Ushkovsky volcano
8-Feb	Orange	EQ (MI 1.4–2.4) T (39.3×10^{-6})	Gas–steam ash	>41 km	Strombolian	Effusion	Lahars	Crater luminescence lava flow luminescence. Ash fallout in Klyuchi
9-Feb	Orange	EQ (MI 1.4–2.4) T (39.3×10^{-6})	Gas–steam ash	>48	Strombolian	Effusion	Lahars	
16-Feb	Orange	EQ (MI 1.7–2.3) T (25.5×10^{-6})	Gas–steam ash	1.3 km	Strombolian	Effusion	Lahars	
4-Mar	Orange	EQ (MI 1.5–2.2) T (15.98×10^{-6})	Gas–steam ash	>20.8 km	Strombolian	Effusion	Lahars	
11-Mar	Orange	EQ (MI 1.5–2.0) T (NA)	Gas–steam ash		Strombolian	Effusion		Ash fallout in Kozyrevsk
12-Mar	Orange Red	EQ (MI 1.5–2.0) T (NA)	Gas–steam ash		Strombolian	Effusion		
14-Apr	Orange Yellow	EQ (MI 1–1.21) T (NA)	Gas–steam					
28-Apr	Yellow	EQ (MI 1–1.19) T (NA)	Gas–steam					
16-May	Yellow	Background	Gas–steam					

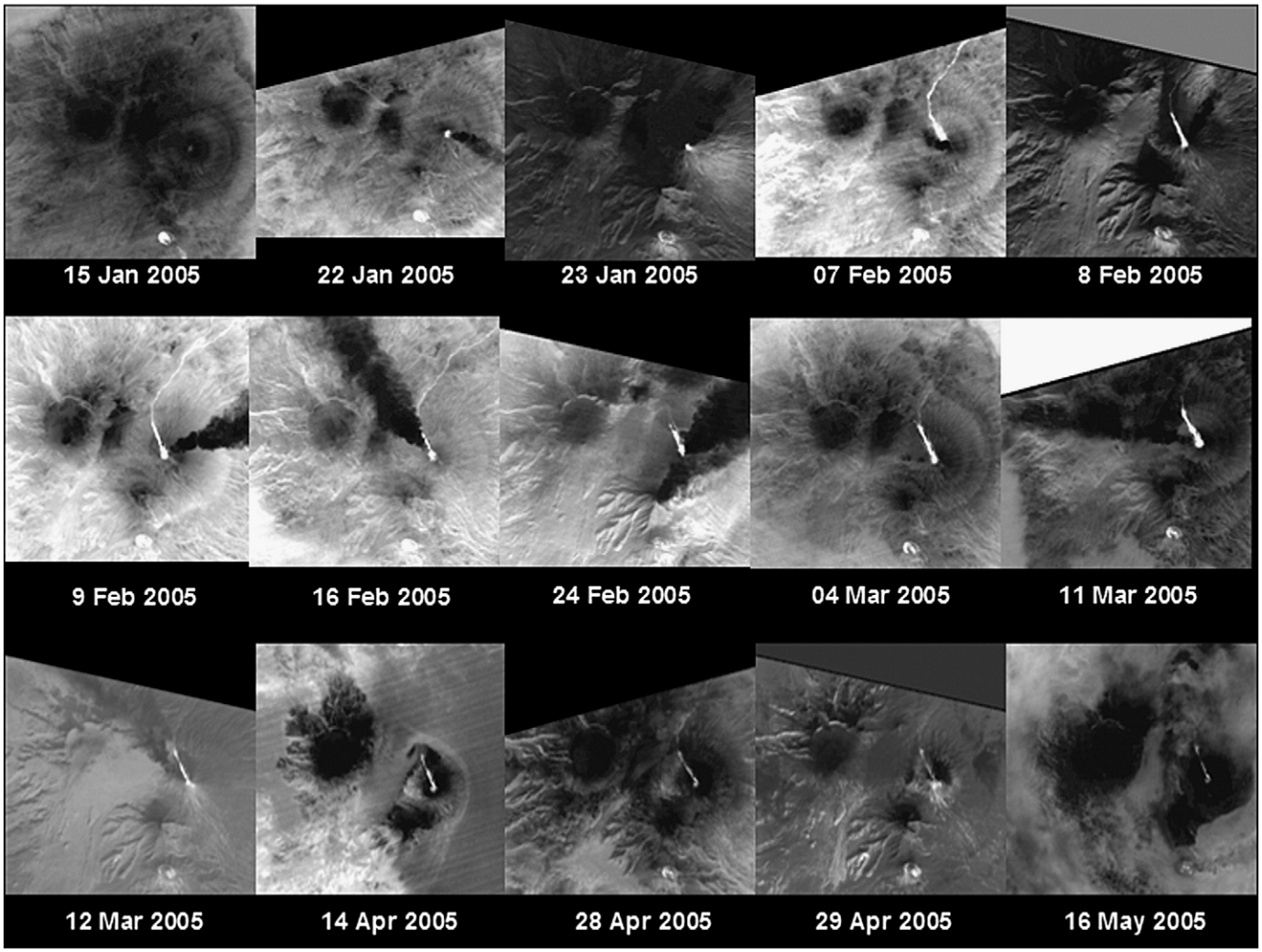

Fig. 3. Time-series of ASTER TIR data of the 2005 eruption of Kliuchevskoi volcano (K), Russia. Data span from the initial thermal anomaly detected on 15 January to the cooling of the lava flow barely visible on 16 May. Also seen are the thermally elevated pixels of Bezymianny Volcano (B) in the early month of the year. Each image is ~50 km wide and rotated with north to the top.

DEM capabilities, as well as multiple bands in the TIR and SWIR regions, which allow for more precise composition, pixel-integrated brightness temperature, and surface property determination. Most importantly, ASTER can be pre-scheduled for various gain settings in the SWIR and VNIR in order to limit data saturation/loss for highly-radiant targets (Pieri and Abrams, 2004). For example, a High gain setting in SWIR Band 9 (2.40 μm) allows for greater sensitivity to targets with lower reflected radiance (~4.0 W m^2 μm^1 sr^{-1}) or slightly warm emission (~86 °C); whereas a gain setting of Low2 for the same band allows unsaturated reflected radiance data to be collected up to ~73 W m^2 μm^1 sr^{-1} or emission up to 329 °C. The TIR subsystem does not have gain settings but has 12-bit quantization, which maximizes the dynamic range and minimizes saturation for most targets. ASTER is the first orbital sensor that provides publicly-available high-spatial resolution data with more than two bands in the TIR region. These data provide the ability to develop new methods for extracting the small-scale compositional and temperature structure of the surface (Ramsey, 2002; Carter et al., 2009; Ramsey and Dehn, 2004).

ASTER is scheduled daily acquiring data for individual user requests, larger-scale global mapping campaigns, as well as emergency acquisitions for events such as volcanic unrest (Yamaguchi et al., 1998). Data can also be acquired in an expedited request mode and processed rapidly (<4 h), which is especially important for response to natural disasters. ASTER has been tasked numerous times in this mode to collect images of volcanic eruptions, forest fires, tsunami and hurricane aftermath, and flooding (Duda and Abrams, 2005; Morisette et al., 2005; Tralli et al., 2005; McAdoo et al., 2007; Carter et al., 2008). In order to utilize this system in the most efficient way possible for restless volcanoes in the north Pacific, a program is now in place whereby thermal anomalies detected by high temporal/low spectral resolution instruments (e.g., AVHRR) trigger an automatic ASTER expedited request (Ramsey and Dehn, 2004; Ramsey et al., 2004). This process has thus far been very successful, resulting in over 100 new ASTER acquisitions of erupting volcanoes since late 2006, including many of the data presented here.

4. Results

4.1. ASTER response and urgent request data processing

The progression of the 2005 Kliuchevskoi eruption was captured with a time-series of ASTER urgent request observations, which spanned the first five months of 2005 (Fig. 3). The first indication in ASTER data that Kliuchevskoi was in the initial stages of an eruption came during a nighttime overpass on 15 January 2005 at 10:55:55 GMT (21:55:55 local time). ASTER was targeted for the continual monitoring of the ongoing eruption of Bezymianny Volcano, 11 km to the south (Carter et al., 2007). Fig. 4 shows both the ASTER TIR and

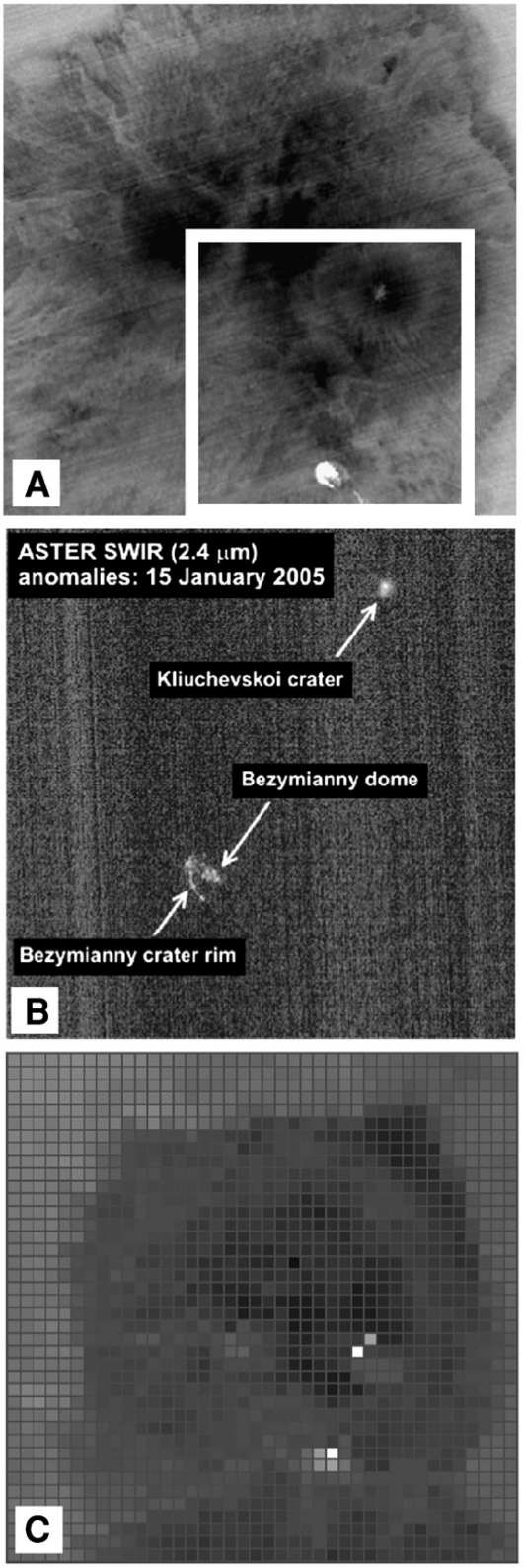

Fig. 4. Thermal anomalies of Kliuchevskoi detected on 15–16 January 2005. (A) Nighttime ASTER TIR acquired on 15 January showing the prominent anomaly at Bezymianny to the south and the faint anomaly at Kliuchevskoi to the north. The white box indicates the area in B. (B) ASTER nighttime SWIR data showing only thermally elevated (>100 °C) pixels at both volcanoes. (C) AVHRR band 3 nighttime data acquired ~16 h later (2:45 GMT) on 16 January. Each gridded bin is a 1 km pixel with thermally anomalies shown at both volcanoes. North is up in each image.

SWIR images from the 15 January acquisition. The dome at Bezymianny is clearly visible in both datasets as is a weaker anomaly at the summit of Kliuchevskoi. ASTER band 9 (~2.4 μm) had saturated pixels, indicating a pixel-integrated brightness temperatures in excess of 97 °C; Urai et al., 1999). However, this activity was not large or hot enough to have triggered a thermal anomaly in the routine monitoring using AVHRR data. It was not until the next day that the activity had increased to a level for an AVHRR band 3 anomalous pixel to be visible (Fig. 4C). The ASTER detection on 15 January and the AVHRR detection the next day triggered a new series of ASTER urgent request observations that continued throughout the eruption and which are documented here.

ASTER level 2 (L2) data (i.e., calibrated, atmospherically-corrected, land-leaving radiance) have been examined in detail in order to determine the relationship of thermal anomalies seen in all three ASTER wavelength regions over time and how these relate to the eruption processes at Kliuchevskoi. Specific ASTER scenes were selected based on several criteria and processed into surface-leaving radiance (AST_09T and AST_09XT). Three criteria used were: a low percentage of cloud cover, the presence of elevated pixel DN values (i.e., thermal anomalies), little to no noise/data loss, and the volcano being centrally-located within each image (Fig. 3). Overall, the time range encompassed the onset of thermal activity at the summit (15 January) until the cessation of lava effusion (16 May), and are summarized in Table 2. As the eruption progressed and active lava flows were emplaced, the radiant pixel-integrated brightness temperature increased significantly allowing progressive detection by the TIR, the SWIR, and finally the VNIR subsystems, which provided a further constraint on the sub-pixel thermal features.

The pixel-integrated brightness temperature, surface composition, and composition of both the plumes were extracted from 10 nighttime TIR datasets. The AST_09T radiance data were used to produce decorrelation stretch (DCS) images, which enhanced the band-to-band emissivity variations, thus revealing the relative compositional differences of the surface units and eruption plumes. A DCS is based upon a principal component analysis of multi-dimensional data, or in this case ASTER TIR datasets. The most correlated data, or principal component, is rotated into the plane of the eigenvector, stretched perpendicularly, and then rotated back to its original axis such that the data can be easily interpreted (Gillespie et al., 1986). The same data were also separated into their temperature and emissivity components using a normalization approach (Gillespie, 1985; Realmuto, 1990; Gillespie et al., 1998; Hook et al., 2005). The average seasonal background temperature was determined for each image by averaging a 40×40 TIR pixel (~13 km^2) area away from the volcanic activity. This value was subtracted from the brightness temperature image, which was then used to identify the location and number of thermally-anomalous (>10 °C above background) features, saturated pixels, and the maximum pixel-integrated brightness temperature in each image.

Nighttime data, with a lack of a solar reflected contribution, are typically ideal for SWIR temperature analysis. However, four daytime SWIR datasets and two VNIR datasets (acquired ~13 h before the nighttime TIR) were also used for temperature analysis presented here. Furthermore the SWIR bands suffer from radiometric errors due to cross-talk contamination between the detectors, which can cause anomalies in the radiance products. The SWIR cross-talk effect can be corrected in the daytime (L2 XT) data products (Iwasaki and Tonooka, 2005). However, nighttime cross-talk corrected data are not available because of the lack of synchronous VNIR data, which are required in the current correction algorithm.

The average reflected radiance from a 30×30 pixel (1.2 km^2) non-volcanic area near the summit was calculated to determine the solar radiance contribution, which was then subtracted from the thermally-anomalous pixels. The solar-corrected radiance images were separated into temperature and emissivity by applying the reference

Table 2
Summary of the ASTER scenes used for this study. Mode: S/T = SWIR/TIR only, Full = VNIR/SWIR/TIR. SWIR Gain factor multipliers: High = 2, Normal = 1, Low1 = 0.75, Low2 = 0.116–0.75). Level 2 (L2) product: AST_09T = ASTER TIR surface radiance, AST_09XT = ASTER SWIR surface radiance (cross-talk-corrected).

Acquisition date	Day/night observation	Data mode	SWIR gain	Pointing angle	Level 1A granule ID	Level 2 (L2) product name
15-Jan-2005	Night	S/T	Normal	2.8	SC:AST_L1A.003:2027471613	AST_09T
22-Jan-2005	Night	S/T	Normal	−5.7	SC:AST_L1A.003:2027574023	AST_09T
23-Jan-2005	Day	Full	High	−5.7	SC:AST_L1A.003:2027560487	AST_09XT
07-Feb-2005	Night	S/T	Normal	−5.7	SC:AST_L1A.003:2027748944	AST_09T
08-Feb-2005	Day	Full	Low 2	−5.7	SC:AST_L1A.003:2027751856	AST_09XT
09-Feb-2005	Night	S/T	Normal	8.5	SC:AST_L1A.003:2027816862	AST_09T
16-Feb-2005	Night	S/T	Normal	2.8	SC:AST_L1A.003:2028177802	AST_09T
04-Mar-2005	Night	S/T	Normal	2.8	SC:AST_L1A.003:2027989033	AST_09T
11-Mar-2005	Night	S/T	Normal	−5.7	SC:AST_L1A.003:2028087206	AST_09T
12-Mar-2005	Day	Full	Low 2	−5.7	SC:AST_L1A.003:2028072076	AST_09XT
14-Apr-2005	Night	S/T	Normal	8.5	SC:AST_L1A.003:2028652072	AST_09T
28-Apr-2005	Night	Full	Normal	−5.7	SC:AST_L1A.003:2028752377	AST_09T
29-Apr-2005	Day	Full	Low 2	−5.7	SC:AST_L1A.003:2028759718	AST_09XT
16-May-2005	Night	S/T	Normal	8.5	SC:AST_L1A.003:2029037490	AST_09T

channel method (Kahle et al., 1980). The resulting temperature images were used to extract maximum pixel-integrated brightness temperatures of the thermal features. The stated geolocation accuracy of the ASTER subsystems (i.e., to within one VNIR pixel), together with the sensitivity of the SWIR data to higher temperatures and its greater spatial resolution, allow for an independent dataset from which to extract the sub-pixel-integrated brightness temperatures and their spatial distribution within the 90 m^2 TIR pixel (Fig. 5). The emissivity spectra extracted from the TIR radiance of pixels with significant sub-pixel thermal heterogeneities are commonly distorted due to the assumption of a single pixel brightness temperature during the emissivity/temperature separation stage (Ramsey and Kuhn, 2004). The ASTER SWIR subsystem with its higher spatial resolution provides for a new methodology, currently being developed, to correct a TIR pixel's distorted emissivity spectrum, which can then be used for accurate compositional analysis.

4.2. ASTER thermal observations

Volcanic unrest at Kliuchevskoi was first reported by KVERT on 12 January 2005 as seismic activity increased substantially (Table 1). In addition, the first observations of a gas–water vapor plume began just a few days prior, on 8 January. As previously mentioned, a nighttime ASTER image acquired on 15 January recorded a thermal anomaly that occupied three 90 m TIR pixels at the summit crater yielding pixel-integrated brightness temperatures between −24 and −22 °C, which were 7 to 9 °C above the average background temperature. A DCS was also performed on ASTER TIR bands 14, 13, and 11 placing them in R, G, B, respectively. A qualitative analysis of the plume can be performed on the resulting color image, with red to reddish-orange color indicating an ash-rich plume, a yellow to yellow–green plume being SO_2-rich, and blue to cyan plume being mostly H_2O-rich (Realmuto et al., 1994, 1997). For the 15 January data, the presence of a small water vapor plume within the summit crater was detected, which corresponded to the sparse ground-based visual observations from observers in Kliuchi.

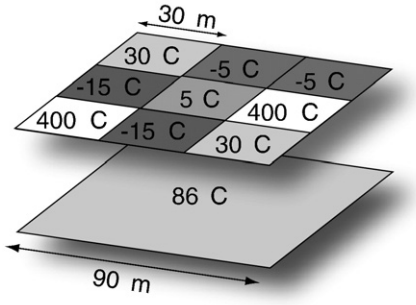

Fig. 5. A simplified sketch demonstrating how the 30 m, high-spatial resolution of the ASTER SWIR subsystem can be used to extract sub-pixel anomalies within one thermally-anomalous, 90 m TIR pixel. Future work will include developing a deconvolution algorithm that will determine areal percentages of hot material within one TIR pixel.

One week later (22 January), ASTER recorded an increase in thermal output at the summit crater of Kliuchevskoi (Fig. 3). Approximately 39 pixels were thermally elevated 10 °C or more above the average background temperature of −37 °C, and 7 of those pixels were now saturated (>97 °C). Recovery pixels (i.e., pixels with no recorded values) were present "down-scan" from the saturated pixels in bands 11 and 12 of the AST_09T radiance data, and confirm a very high level of radiance was recorded in the adjacent pixels. A linear feature extending to the southeast from the summit crater was analyzed using the DCS approach and found to be a 1.8 km by >10.6 km long SO_2-rich (green) plume containing ash (red) east–southeast of the summit. Above the summit, the plume appears to be primarily composed of water vapor (blue). Daytime SWIR data, collected 12 h later on 23 January, also revealed the presence of recovery pixels and 150 saturated pixels (temperatures >410 °C) in band 4 that occupied an area 0.135 km^2. The gas–water vapor plume could be seen extending to the northeast from the summit crater. The saturated pixels present in the SWIR subsystem meant temperatures were now very high in the summit crater most likely from a small actively-overturning lava lake or vigorous Strombolian activity. A maximum pixel-integrated brightness temperature of 806 °C was extracted from solar-corrected VNIR band 3 (0.807 μm) data.

On 7–9 February, a unique ASTER observational opportunity occurred. The high latitude of Kliuchevskoi, combined with the orbital configuration of the Terra satellite and the off-nadir pointing ability of the ASTER sensor, allowed for a consecutive night–day–night observation sequence. Two nighttime SWIR/TIR datasets and one daytime VNIR/SWIR/TIR dataset were collected. The 7 February nighttime TIR image had a large thermal anomaly along the NW flank, partially obstructed from view at the summit by a 4.1 km long plume that was composed of relatively equal amounts of ash and SO_2. The thermal feature consisted of hundreds of pixels thermally elevated at least 10 °C above background (−31 °C), 10 pixels at or above the TIR saturation temperature (97 °C), and an associated water vapor signature in the DCS image. The daytime SWIR pixel-integrated brightness temperatures extracted from the 8 February data had a maximum pixel-integrated brightness temperature at or above saturation (467 °C in band 4). A linear stretch of the concomitant VNIR pixels shadowed by the upper portion of the volcano revealed incandescence within the Krestovsky channel. The thermally elevated TIR and SWIR pixels were overlain onto the VNIR data for comparison and showed that the majority of saturated TIR and SWIR pixels were located on/near the incandescent pixels. The maximum VNIR brightness temperature was 807 °C corresponding to the open-channel lava flow. On the night of 9 February, the eruption plume had the

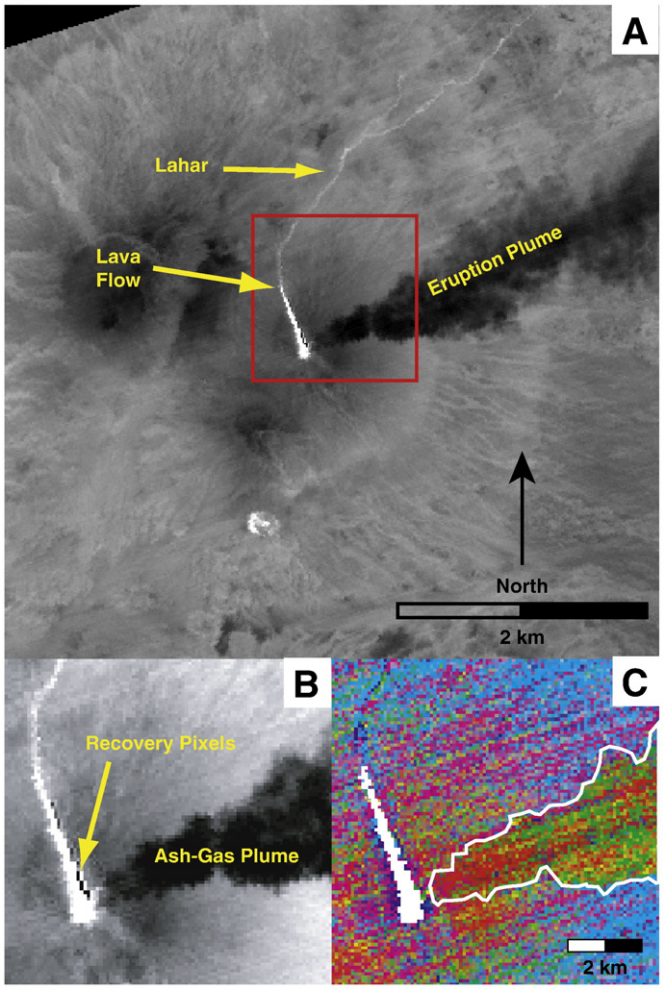

Fig. 6. ASTER TIR data of Kliuchevskoi acquired on 9 February. (A) ASTER TIR band 10 radiance image. The lava flow, lahar, and cooler eruption plume are visible. The red box highlights the area in B and C. (B) Zoomed image showing the filled crater, lava flow and recovery pixels associated with adjacent saturated pixels. (C) A decorrelation stretch image of ASTER TIR bands 14, 13, 11 in R, G, B, respectively. Ash-rich portions of the plume are red, SO_2-rich portions are green/yellow, and water vapor is blue. This image shows a gradation from an ash-rich plume near the summit to prominently SO_2 distally as fallout occurs in addition to localized water vapor plumes along the perimeter of the thermally-anomalous region (white).

same composition observed previously, however it had shifted to the NE and extended >40 km off the image (Fig. 6). This shift allowed for an unobstructed view of the thermal anomaly at the summit region, which had a total of 35 TIR pixels above saturation. The prominent thermal feature was now 600 to 900 m wide and extended ~2.0 km from the summit crater where it tapered to a width of 100 to 300 m. Below this feature a thin and much cooler (−25 °C; ~10 °C above background) linear feature (presumably a lahar deposit) extended ~27 km to the NW terminating in the Kruten'kaya River.

On 16 February a decrease in saturated TIR pixels from 35 to 11 was observed within and near the summit crater along with one associated recovery pixel. The dimensions of the large thermal anomaly were ~670 m across near the summit and 100–350 m across approximately 1 km down slope. A plume extended to the NW for >48 km, and partially obstructed the view of the narrowest portion of the anomaly. The plume composition had also changed from prior analyses becoming more ash-rich near the summit with an overall transition to SO_2 distally. Similarly, smaller plumes were observed along the thermal anomalies on the NW flank and within the summit crater. The low-temperature, linear thermal anomaly was also visible with a consistent pixel-integrated brightness temperature from previous data of around −25 °C. Unfortunately, a daytime observation was not available around this time in order to produce a L2 SWIR and VNIR dataset.

The next successful nighttime ASTER acquisition was on 4 March and a significant change was noted with 373 TIR pixels being thermally elevated over the background (−35 °C). In total, there were 39 saturated pixels and 6 recovery pixels with the remainder of the prominent thermal feature brightness temperatures ranging between −22 and 97 °C. Previously, the anomaly was measured at ~100 m across at the narrowest segment but had now increased to ~600 m. The length of the widest portion was 2.9 km with an additional 1 km segment exhibiting two tail-like features further down slope. The northern tail extends roughly 10 km, whereas the southern tail ends abruptly at 760 m. A continuous plume was no longer visible, however two small dark puffs (1.3×0.8 km) west of the summit and along the thermal anomaly were detected. The puffs contained a mixture of ash and SO_2, whereas the plumes along the flank appear to be a mix of ash and water vapor.

The thermal anomaly that had extended ~4.6 km NW of the summit began to decrease in temperature, but was still visible in the TIR and SWIR data acquired on 11 and 12 March, respectively. Collectively, 196 pixels were >10 °C above the background temperature (−16 °C; Fig. 3) in the nighttime TIR data. In the summit crater area and upper elevations of the Krestovsky channel, 40 of those TIR pixels were at or above saturation. Most notably, the linear feature along the lower elevations was no longer visible except for a ~1.3 km tail-like portion at the terminus of the main anomaly. Daytime SWIR data acquired ~12 h later showed 49 pixels greater than 378 °C (saturated band 6) over the summit and upper channel, similar to the 11 March data. However, a maximum VNIR brightness temperature was not obtained and no visible incandescence was observed indicating that the lava had cooled significantly. Seismic data included within the KVERT information releases (Table 1) show decreasing volcanic tremor between 9 February and 12 March, and corresponds with a cessation in lava effusion by that time.

The remaining ASTER data (14 April 14, 28 and 29 April, and 16 May) showed a steady decrease in the pixel-integrated brightness temperature of the thermal features. It should be noted that a significant increase in volcanic tremor occurred on 23 March when it reached a maximum value of 6.2×10^7 μm/s that resulted in a color code change from orange to red. Over a 2-day period the volcanic tremor steadily decreased and the color code was lowered to orange by 28 March. Unfortunately, a cloud free ASTER acquisition was not available until 14 April to determine the true thermal response and eruptive processes at the surface during this time. By mid-April saturated TIR pixels were no longer present in the summit crater or along the flanks. The pixel-integrated brightness temperatures of the anomaly were much cooler than the two previous months ranging from −15 °C along the Krestovsky channel to 3.6 °C in the summit crater on 14 April. At this time, the total length was roughly 4.3 km and varied in width from 200 m near the base to 600 m at the summit. A nighttime TIR acquisition on 28 April had numerous pixels throughout the image at 10 °C above background (−24 °C). One pixel located within the summit crater area produced a maximum TIR pixel-integrated brightness temperature of 2.8 °C, whereas a daytime overpass on 29 April had a maximum SWIR brightness temperature of 173.7 °C (band 6) due to the greater sensitivity of the target's radiance in the SWIR wavelength region. Although the length of the anomaly remained relatively unchanged in the 16 May scene, the width steadily decreased to 470 m at its widest, and the pixel-integrated brightness temperatures ranged between −19.5 and −3.3 °C. These were beginning to approach equilibrium with seasonal background temperatures. Throughout the months of April and May no plume was detected in the TIR data (Fig. 3).

Table 3
Summary of the saturated daytime SWIR pixels recorded by ASTER throughout the 2005 eruption of Kliuchevskoi volcano. This table shows the original pixel counts for each daytime acquisition under a High gain in January and Low2 gain for the remaining datasets as well as a corrected pixel count once the data was normalized to a High gain setting. A summary of the calculated lava volumes extracted from the normalized saturated SWIR pixels reveals a consistent decrease between 23 Jan and 12 Mar in spite of the initiation of effusion at the end of January.

	23-Jan	8-Feb	12-Mar
Original pixel count	150	257	9
Corrected pixel count	150	263	9
Erupted volume (km^3)	0.01271	0.0095	0.0013

4.3. Eruption rate

In order to determine a proxy for lava effusion throughout the eruption, the number of saturated SWIR pixels (Band 4) for each daytime scene was recorded (Table 3). If one assumes that the saturated SWIR pixels correlate to lava flows with little to no crust, then the surface area of those flows can be easily extracted from the ASTER data. In order to calculate lava volume, an estimate of depth must be made. Ozerov et al., 1997 documented lava flow thicknesses for Kliuchevskoi volcano ranging between 2 and 25 m. The latter was used here to establish a maximum possible volume. Furthermore, to approximate the shape of the nested summit crater and Krestovsky channel, a disk and half elliptical tube cross-cut through the long axis were used. Although ASTER has DEM capabilities, the available data could not be used here due to a calculated vertical resolution of 20 m with 95% confidence (Fujisada et al., 2005), roughly the maximum thickness of the lava flows.

Because the three SWIR datasets were acquired with different gain settings (and therefore a possibility of more or less saturated pixels), a correction factor was applied in order to scale between data collected. The 8 February and 12 March datasets were acquired in Low2 gain, whereas the 23 January dataset was in High gain. In order to normalize the difference between the Low2 and High gain settings, band 4 in each dataset was multiplied by its associated gain factor, and a common non-thermally elevated pixel for each scene was located. The difference in radiance values for this common pixel was used to scale the Low2 data into High gain. The corrected scenes were then divided by the new gain factor (High gain; 2) resulting in the same radiance value for the common non-thermally elevated pixel. Lastly, saturated pixels were counted for each dataset (Table 3). The newly determined saturated pixel count was used to estimate the area of active lava within each SWIR scene. These areas were then converted into volumes by multiplying the assumed depths of the channel and summit crater. On 23 January, a total volume of 1.27×10^{-2} km^3 was present within the nested summit crater. Although effusion began shortly thereafter, the total volumes calculated for 8 February and 12 March decreased steadily to 9.50×10^{-3} km^3 and 1.30×10^{-3} km^3, respectively. In total, the ASTER data over this 3 month time period suggests approximately 2.35×10^{-2} km^3 of material was erupted at the summit of Kliuchevskoi.

4.4. ASTER emissivity observations

Emissivity spectra of two samples collected within the Krestovsky channel during the August 2005 field campaign were determined in the IVIS laboratory at the University of Pittsburgh. These spectra were degraded to the spectral resolution of the ASTER TIR and compared to the TIR-derived emissivity spectra of an isothermal, non-thermally elevated pixel from the 9 February image (Fig. 7). Sample Klyuch-01-05 is a blocky, massive non-vesicular basalt, whereas Klyuch-02-05 is a basaltic bread crust block. Sample Klyuch-01-05 produced a spectrum remarkably similar to the ASTER-derived data yielding a maximum emissivity difference ($\Delta\varepsilon$) of 0.023 in ASTER band 14. Although Klyuch-02-05 has a slight inversion between ASTER bands 11 and 12 (Fig. 7), the maximum $\Delta\varepsilon$ compared to the isothermal ASTER pixel was also minimal (0.016) and indicates good agreement between the laboratory-derived and remotely sensed spectra.

A thermally elevated ASTER pixel, located along the active lava flow on the northwestern flank was also chosen for comparison to the laboratory-derived basalt spectra. Although the overall spectral shape remains consistent with the lab spectra, especially in ASTER bands 10 and 11, a significant increase in $\Delta\varepsilon$ is observed in the ASTER spectrum as wavelength increases (Fig. 7). A maximum $\Delta\varepsilon$ of 0.042 occurs at band 13 between the ASTER pixel and sample Klyuch-01-05, whereas the same band produces a maximum $\Delta\varepsilon$ of 0.036 for sample Klyuch-02-05. This error is the direct result of a TIR pixel with significant sub-pixel thermal heterogeneity being treated as isothermal during the separation of emissivity from temperature. Such an assumption is unavoidable and produces data that are easily identified as thermally mixed. However, in order to correct these distorted emissivity spectra further corrections and/or examination of the SWIR data is required. Collectively, comparisons between the lab derived and ASTER spectra exhibit good correlation with respect to composition, but clearly show errors commonly associated with thermally elevated features.

5. Discussion

5.1. Thermal data

During the 2005 eruption of Kliuchevskoi volcano, 6 saturated TIR pixels (0.05 km^2) were first observed on 22 January and increased to a maximum of 40 pixels (0.32 km^2) by 11 March (Fig. 3). Similarly, the SWIR subsystem also saturated during this time, although the same pattern is not observed as in the TIR. A peak of 257 SWIR pixels (0.34 km^2) occurred in the 8 February dataset and decreased to 49 pixels (0.04 km^2) by 12 March. By utilizing the VNIR subsystem of ASTER, maximum pixel-integrated brightness temperatures of 808 and 806 °C were extracted in the 22 January and 8 February data during which time incandescence was also reported by KVERT. Such high temperatures in conjunction with saturation of the TIR and SWIR suggest that the thermal anomalies within the summit crater and Krestovsky channel were produced by open-channel lava effusion rather than high temperature fumaroles.

The discrepancy between the timing of peak TIR and SWIR areas of saturation (Fig. 8) is most likely the result of the lava flows simply being obscured by the shifting eruption plume. Moreover, the SWIR data may be recording peak open-channel lava effusion during the 8

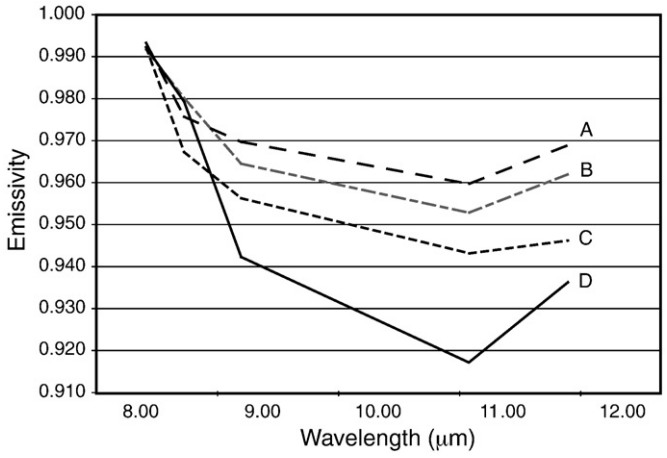

Fig. 7. Summary of emissivity spectra obtained from two samples collected in the field in addition to spectra extracted from both thermally elevated and non-thermally elevated TIR ASTER pixels. A = Sample Klyuch-02-05 bread crust basalt; B = Sample Klyuch-01-05 blocky basalt; C = Non-thermally elevated, isothermal ASTER spectrum; D = Thermally elevated, non-isothermal ASTER spectrum. The data show how the presence of thermally-mixed pixels results in large errors of emissivity spectra and support the development of a deconvolution algorithm.

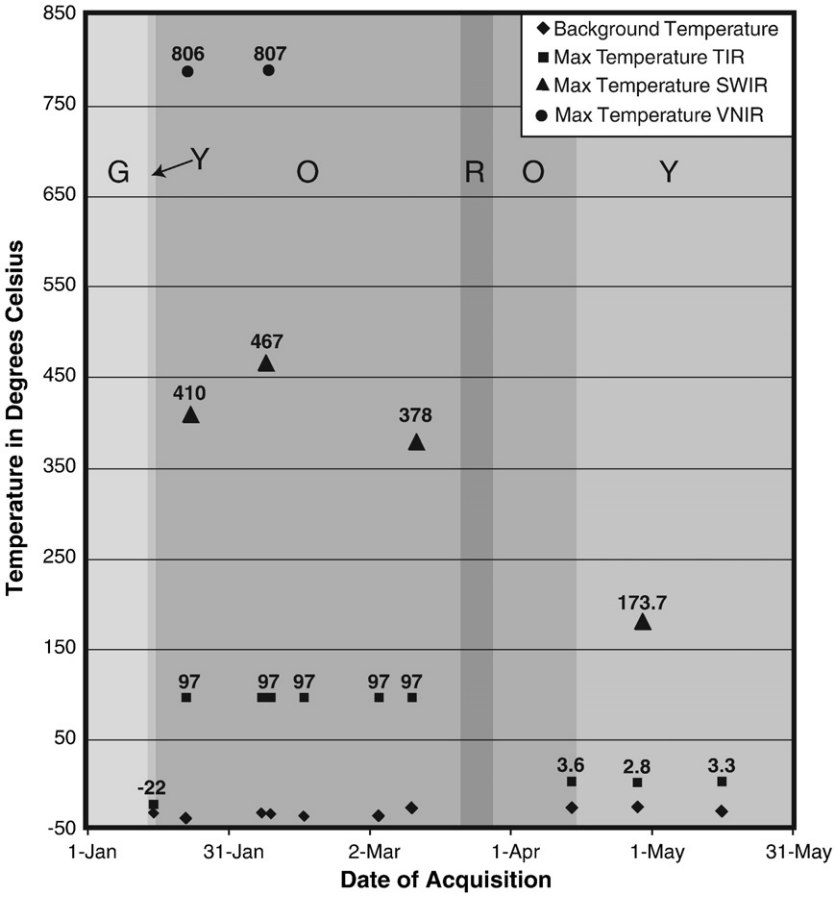

Fig. 8. Summary of the 2005 Kliuchevskoi eruption pixel-integrated brightness temperatures derived from ASTER. Band 10 (TIR; squares), bands 4 and 6 (SWIR; triangles), and band 3 (VNIR; circles) from each subsystem were used. The data reveal a maximum temperature above saturation of both the TIR and SWIR subsystems starting on 8 Feb. Band 4 was used to determine maximum SWIR temperatures on 23 Jan and 8 Feb and variable saturation between acquisitions is a result of a High gain and Low2 gain setting, respectively. Band 6 was used for the 12 Mar and 29 Apr acquisitions and also had a Low2 gain setting. The average background temperatures derived from the TIR (diamonds) are shown for reference, as is the KVERT color code in the background. A brief period of heightened seismicity (R) was reported by KVERT between 24 and 28 March. R = Red, O = Orange, Y = Yellow, and G = Green (KVERT color codes).

February acquisition and subsequent formation of a partial lava flow crust by 12 March. The VNIR data could not be used to determine brightness temperatures subsequent to the 12 March acquisition due to the decreasing pixel-integrated brightness temperatures. We attribute this to the closing off of the open-channel and the formation of insulating lava tubes. These crusted surfaces were still hot enough to allow saturation of the SWIR pixels (467 °C), but cooler than the lower limit of the VNIR detection (705 °C). These results are in agreement with KVERT reports that document the presence of lava flows on 15 and 20 March, but do not specify if they are active (Table 1). Moreover, the information releases correspond well with our interpretations of the ASTER data as they first reported incandescence within the crater initiating on 16 January, Strombolian activity on 20 January, and lava effusion from 31 January until 8 March.

The lava volumes calculated by using radiance observations for the three daytime SWIR datasets indicate an ASTER-perceived overall decrease within a three month period. However, the 8 February SWIR image shows the onset of an effusive stage of the eruption implying that an increase in lava volume should be expected. The decrease in lava volume from 23 January to 8 February may be the result of three possible factors: 1) The correction for the gain normalization between datasets may contain inherent errors whereby the solar azimuth, solar elevation, and seasonal variation between datasets could have resulted in an initial difference in radiance values for the pixels targeted; 2) Just prior to the 8 February acquisition, a cooled-carapace and/or lava tubes may have formed on the surface of the lava flow that prevented saturation of the SWIR data, thereby minimizing the total surface area of the active flow; 3) In the 8 February SWIR image, the active lava within the summit crater appears to have reduced in size from 23 January and suggests that the lava lake has drained and/or cooled once effusion began in the Krestovsky channel.

Further examination of the saturated SWIR pixels in the 8 February dataset reveals a detachment between the nested summit crater lava pond and the lava flow within the Krestovsky crater, suggesting that the lava flow originated from a breakout point below the elevation of the nested summit crater. This may be due to a structurally weak zone at or near the summit, a feeder dike rooted from the main conduit, or development of a lava tube. During the August 2005 field investigation, a helicopter over flight and a Forward Looking Infrared (FLIR) camera were used to evaluate the thermal conditions of the volcano. This FLIR data (Fig. 9) confirms the presence of a breakout point approximately 90 m below the rim of the nested summit crater, and does not reveal the presence of thermal anomalies within the main crater that would indicate a flow had breached the nested summit crater and travelled down the Krestovsky channel. Pixel-integrated brightness temperatures within the main summit crater remained at background levels (approximately −9 °C + /− 5 °C) whereas the lava flow and portions of the nested crater had maximum brightness temperatures in excess of 100 °C over 6 months following emplacement. These data, in conjunction with volume change observations,

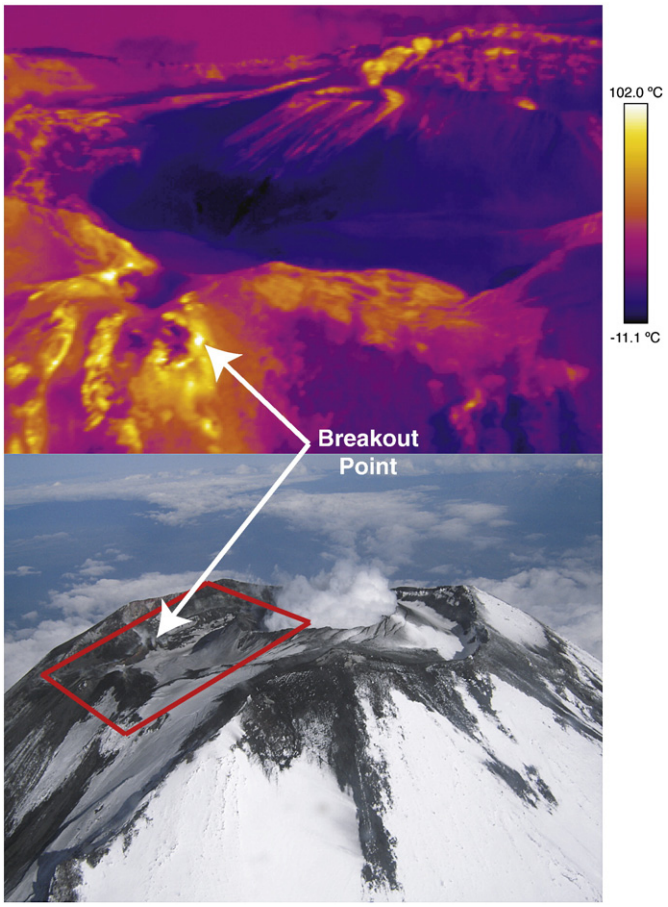

Fig. 9. A comparison between a FLIR image and a digital photo of the summit of Kliuchevskoi, taken during a post-eruption overflight in August 2005. Red box shows coverage of the FLIR image with the breakout point highlighted by white arrows. The high-spatial resolution of the FLIR data reveals a breakout point for the effusion of lava on the top northwestern flank in the Krestovsky channel, possibly due to a structurally weak zone in the summit region. White/yellow = hot pixels; Black/blue = cold pixels.

suggest that the lava lake within the summit crater drained either back into the main conduit, or into a weak fractured zone that rerouted the lava to the breakout point at the top of the Krestovsky channel.

5.2. Composition from the TIR

Gillespie et al., 1998, introduced a temperature and emissivity separation algorithm for ASTER data capable of determining pixel-integrated brightness temperatures of the surface to within 1.5 K and mineral compositions to within an emissivity error of 0.015. However, this algorithm (like all temperature/emissivity separation techniques) is constrained by assumptions of a homogeneous and isothermal Lambertian surface emitting equally at all angles over a 90 m by 90 m area. Previously, deconvolution or spectral unmixing algorithms have been developed and applied to the extracted emissivity for geologic applications (Adams et al., 1986; Gillespie, 1992; Johnson et al., 1992; Sabol et al., 1992; Ramsey and Christensen, 1998; Ramsey and Fink, 1999; Zorn and Ramsey, 2002) in order to determine mineral and textural abundances in spectrally-mixed TIR pixels. These approaches fail however where isothermal conditions are not present (Ramsey and Dehn, 2004; Ramsey and Kuhn, 2004). Unlike ASTER pixels with varying compositions that produce linearly mixed emissivity spectra, the non-isothermal pixels behave non-linearly producing large errors in slope of emissivity versus wavelength plots (Fig. 7). The conditions on Kliuchevskoi that produced the slope in the emissivity spectra are related to one of the following: 1) A portion of the pixel contains active lava as well as ambient surface material; 2) Hot cracks may have formed on a cooling carapace of the lava flow; and/or 3) Hot fumaroles may be scattered across the northwestern flank. Future work will attempt to utilize data from all three subsystems of ASTER in order to develop a thermal deconvolution algorithm capable of extracting the temperatures and areal percentage of hot material in mixed TIR ASTER pixels for the purpose of correcting the emissivity spectra.

Information extracted from the decorrelation stretch of the ASTER TIR data also allowed for compositional discrimination of the plumes throughout the 2005 eruption. Plumes were present in each acquisition and were typically located within the summit crater and along the lava flows in the Krestovsky channel. The plumes within the summit crater appear to be persistent throughout the eruption and are probably related to degassing of magma, fumarolic activity, and the melting of snow and ice during heating events. During effusive activity, KVERT reported phreatic explosions and lahar production within the Krestovsky channel as a result of lava interaction with snow and ice. This activity supports the interpretation of the presence of water-rich plumes along the lava flows.

Based upon information releases by KVERT, ash fallout occurred on 7 February on the southwest flank of nearby Ushkovsky volcano, in the town of Klyuchi on 9 February, and in the town of Kozyrevsk on 11 March (Table 1). The ASTER TIR data agrees with these reports and showed an ash depletion signature of the eruption plume as it migrated away from the summit crater. Additionally, the 22 January and 16 February ASTER data had a similar ash fallout signature. The 4 March acquisition does not exhibit this type of plume activity. However, it does reveal a series of isolated ash/SO_2 puffs commonly associated with Strombolian explosions during gas-rich magma resupply (Ripepe et al., 2002). This interpretation is also consistent with the KVERT seismic data that showed a dramatic increase in activity at this time.

5.3. Limitations

This study has produced results, which are in agreement with the observations documented by KVERT. However, some limitations of extracting critical information were identified. First, the extreme topographic relief of Kliuchevskoi combined with varying look angles between the day and night ASTER acquisitions (Table 2) resulted in a parallax error at the highest elevations even following geometric correction and using orthorectified data. This error prevented precise pixel-to-pixel comparisons between the VNIR, SWIR, and TIR data thereby limiting certainty of spatial comparisons to within one 90 m TIR pixel as opposed to the standard 15 m registration error for regions of little topographic relief.

In order to minimize this problem in the future, two approaches may be used: 1) use only daytime or nighttime acquisitions, such that the look angle remains constant between the subsystems; 2) collect a well-distributed series of ground control points on or near the summit and the surrounding plain so that images can be geolocated to compensate for parallax and geometric distortions; and/or 3) concentrate on determining sub-pixel temperature extraction where relief and distortion is minimal. Of these, the first appears to be most feasible although it does limit the amount of data available for analysis. Collecting ground control points in such a remote and topographically-extreme area includes numerous logistic issues, and applying sub-pixel temperature extraction on volcanic areas of little relief is relatively simplistic and limiting. Therefore, in order to characterize the eruptive behavior of large, dangerous volcanoes such as Kliuchevskoi using all possible ASTER data, future work must include a more robust topographic and data geolocation approach.

Other limitations are inherent in the ASTER data. The daytime SWIR and VNIR data contain a mixture of emitted radiance from the lava flows and solar reflected radiance, but are able to have the cross-

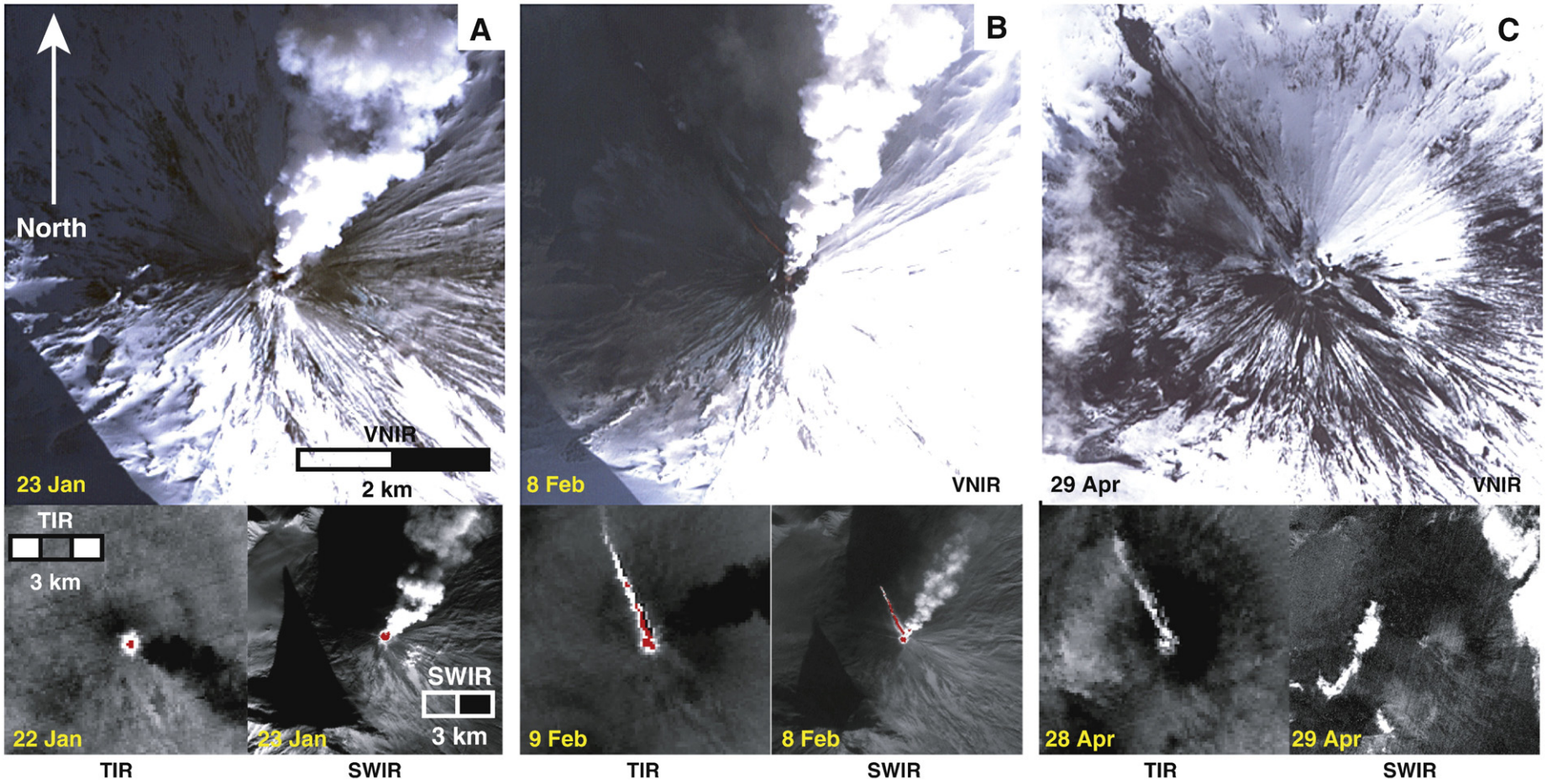

Fig. 10. An eruptive phase summary of the 2005 Kliuchevskoi eruption as observed by the 3 subsystems of the ASTER instrument. These datasets reveal an (A) explosive (B) explosive–effusive and (C) cooling phase. Saturated TIR and SWIR pixels are shown in red in addition to the associated recovery pixels shown in black along the flows. Spatial scale is consistent between each phase and subsystem.

talk error removed from the SWIR data. Conversely, the nighttime SWIR data are free of solar contamination, but remain uncorrected for the cross-talk error because coincident VNIR data, needed for the correction, are not present. The contributions of solar reflected radiance to the maximum derived brightness temperatures is only an approximation and can have associated errors due to over or under-correcting for this variable. In this study, over-compensating for solar reflected radiance results from subtracting an average background value that is higher than the true radiance and ultimately produces maximum brightness temperatures that are too low (for what is expected for these active lava flows as well as the detection thresholds of ASTER). The opposite is true for instances of under-correcting as well, and suggests that a logical correction of solar reflectance will result in relatively small errors (as little as 0.3 °C) in the derived pixel-integrated brightness temperatures of highly-radiant targets approaching saturation. However, as surface temperatures decrease, errors in resultant brightness temperatures of the SWIR also increase significantly (up to 130 °C). These error values were determined by subtracting a minimum and maximum average solar radiance value from the image, subsequently processed into an integrated brightness temperature image, and compared to the integrated brightness temperature images used for this investigation. Ultimately, the errors associated with solar correction, geolocation, and cross-talk correction all propagate into the derived brightness temperature calculations and introduces future obstacles in the precise and accurate deconvolution of thermally-mixed pixels in order to extract accurate surface compositional/textural information of hot targets.

Previous work has compared two primary methods developed to minimize errors associated with solar reflected radiance: a mean background subtraction and per-pixel correction (Wooster and Kaneko, 2001). Although that study found the per-pixel method to be more robust, the results were for a dacitic surface with much cooler carapace temperatures. In the SWIR, the spectral reflectance of dacite lavas are twice that of basalt lavas and, therefore, require higher surface temperatures (>30 °C) than basaltic rocks in order to isolate their thermal signal from the solar reflected signal. Essentially, surfaces with basaltic compositions are less susceptible to errors associated with solar reflectance in general (Wooster and Kaneko, 2001). The maximum pixel-integrated brightness temperatures of the basalt lava flows presented here are ~800 °C, and are significantly higher (>30 °C) than the dacite temperatures observed in Wooster and Kaneko, 2001. This suggests that the solar corrections applied to the daytime datasets had minimal affect on the resulting brightness temperatures of the hot pixels.

To minimize the errors associated with solar reflected surface radiance, the use of nighttime data is preferred. However, these data present the aforementioned issues of cross-talk as well as larger geolocation errors due to the lack of the VNIR data and inability to know precisely the amount of error involved in geolocating the SWIR and the TIR images. Future work will continue attempts to acquire nighttime data in addition to utilizing the "per-pixel" approach to correct for reflected solar radiance in daytime SWIR and VNIR data. In addition, an error analysis of using the daytime versus the nighttime SWIR/TIR data will be needed incorporating all the errors from cross-talk to geolocation to solar reflection.

6. Conclusions

The behaviors described here for the 2005 Kliuchevskoi eruption are analogous to those observed in previously documented summit eruptions in that this summit eruption included Strombolian activity, lahars, and phreatic explosions along the flanks. Large ash plumes produced during this event and extending more than 300 km from the volcano corroborate assertions by others as to why monitoring of Kliuchevskoi is essential for aircraft safety. The 2005 eruption of Kliuchevskoi volcano was monitored and observed using the ASTER instrument and supplemented by information releases provided by KVERT. Collectively, these data revealed three phases of activity, including a precursory, explosive, and explosive–effusive phase as the eruption progressed over a five month long period (Fig. 10). On 12 January, seismic activity increased above background levels followed by gas–water vapor emission and the onset of a summit thermal anomaly within the main crater by 15 January. We interpret this activity as a precursory signal for an impending eruption.

Over the course of five days, the precursory phase transitioned into a vigorous explosive phase of activity associated with Strombolian explosions within the summit crater as well as a continued increase in seismic signals. This explosive phase of the eruption monitored by the ASTER instrument is characterized by the presence of saturated TIR and subsequently SWIR pixels as magma began to rise to shallower levels. Decorrelation stretch images performed on the TIR radiance datasets reveal that explosive activity is associated with a transition from gas and water-rich plumes to ash-bearing plumes (Fig. 10). Furthermore, the ASTER instrument allowed for identification of explosive activity by recording the presence of incandescence within the summit crater, which was also concurrent with a strong seismic signal reported by KVERT.

The final explosive–effusive stage of eruptive activity is distinguished by a significant increase in the number of saturated ASTER TIR and SWIR pixels. In addition, a peak in seismic signal intensity related to the initiation of lava effusion from the summit crater is also observed (Table 1). Visible incandescence within the summit crater (Fig. 10) and within the area of TIR and SWIR saturation is observed in the VNIR datasets as maximum pixel-integrated brightness temperatures of the basalts are in excess of 800 °C. Moreover, the lava effusion likely melted snow cover and produced water vapor plumes along the flows, an SO_2 plume extending from the summit crater, and cooler lahar signals emanating from the toes of the flows.

Collectively, the thermal and seismic data show a correlation between the color code advisory and maximum pixel-integrated brightness temperatures recorded by the ASTER instrument, whereby the highest temperatures occurred during lava effusion and elevated seismic activity. The first thermal anomaly recorded by ASTER occurred on 15 January, and the following day the color code was raised to orange. Between the 14 April and 16 May acquisitions, the general pattern of maximum temperatures of the eruption suggest steady cooling of the lava flows as well as decreased thermal activity within the crater, as the areal expanse of the anomalies decreases. Furthermore, KVERT information releases report decreased seismic activity and a cessation of Strombolian activity by the end of April, also in agreement with the ASTER observations presented here.

Field observations including a high-spatial resolution FLIR camera, conducted in August 2005 and 2007 will be used to supplement results presented here in order to further elucidate compositional and thermal variables below the inherent spatial resolution of the ASTER instrument. Although, further image processing is needed to correct the thermally-mixed data, extract accurate compositional and temporal information, and precisely characterize the inherent radiometric and geometric errors, this work provides a foundation for similar thermal/compositional monitoring of ongoing eruptions around the world using ASTER or future instruments with similar characteristics.

Acknowledgements

This work was funded by NASA grants NNG04G069G and NNX08AJ91G, in addition to a University of Pittsburgh International Studies Fund (ISF) grant (Ramsey and Rose, 2005). Assistance for the field and logistical planning was provided by E. Gordeev, O. Girina, O. Evdokimova, and A. Ozerov from the Institute of Volcanology and Seismology (VS) of Petropavlovsk-Kamchatsky, Russia. We would also like to thank R. Wessels, J. Eichelberger, P. Izbekov, and M. West for field assistance and logistics.

References

Adams, J.B., Smith, M.O., Johnson, P.E., 1986. Spectral mixture modeling: a new analysis of rock and soil types at the Viking Lander I site. Journal of Geophysical Research 91, 8098–8112.

Carter, A.J., Ramsey, M.S., Belousov, A.B., 2007. Detection of a new summit crater on Bezymianny Volcano lava dome: satellite and field-based thermal data. Bulletin of Volcanology 69 (7), 811–815.

Carter, A.J., Girina, O., Ramsey, M.S., Demyanchuk, Y.V., 2008. ASTER and field observations of the 24 December 2006 eruption of Bezymianny Volcano, Russia. Remote Sensing of Environment 112 (5), 2569–2577.

Carter, A.J., Ramsey, M.S., Durant, A.J., Skilling, I.P., Wolfe, A.L., 2009. Micron-scale roughness of volcanic surfaces from thermal infrared spectroscopy and scanning electron microscopy. Journal of Geophysical Research 114, B02213. doi: 10.1029/2008JB005632.

Casadevall, T.J., 1993. Volcanic ash and airports — discussion and recommendations from the workshop on impacts of volcanic ash on airport facilities. U.S. Geological Survey Open-File Report, vol. 93–518, p. 52.

Casadevall, T.J., 1994. The 1980–90 eruption of Redoubt volcano, Alaska: impacts on aircraft operations. Journal of Volcanology and Geothermal Research (Special Issue) 62 (1–4), 301–316.

Chebrov, V., 2008. Complex seismological and geophysical investigation of Kamchatka and Commander Islands. In: Chebrov, V. (Ed.), Annual report of KB GS RAS, p. 268 (in Russian).

Dehn, J., Dean, K., Engle, K., Izbekov, P., 2002. Thermal precursors in satellite images of the 1999 eruption of Shishaldin Volcano. Bulletin of Volcanology 64 (8), 525–534.

Duda, K.A., Abrams, M., 2005. ASTER and USGS EROS disaster response: emergency imaging after hurricane Katrina. Photogrammetric Engineering and Remote Sensing 71, 1346–1350.

Eichelberger, J.C., Eichelberger, L.G., 2008. Volcanism in Kamchatka, Russia. American Geophysical Union, Fall Meeting Abstracts, No. V41E-01.

Fedotov, S.A., Masurenkov, Y.P., 1991. Active Volcanoes of Kamchatka, vol. 1. Nauka, Moscow, p. 713.

Fedotov, S.A., Khrenov, A.P., Zharinov, N.A., 1987. Klyuchevskoy Volcano, its activity in 1952–1986 and possible evolution. Volcanology and Seismology 6, 3–17 (in Russian).

Fujisada, H., Bailey, G., Kelly, G., Hara, S., Abrams, M., 2005. ASTER DEM performance. IEEE Transactions on Geoscience and Remote Sensing 43, 2707–2714.

Gillespie, A.R., 1985. Lithologic mapping of silicate rocks using TIMS. The TIMS Data Users' Workshop. JPL Publication 86–38, Jet Propulsion Laboratory, Pasadena, CA, (pp. 29–44).

Gillespie, A., 1992. Spectral mixture analysis of multispectral thermal infrared images. Remote Sensing of Environment 42, 137–145.

Gillespie, A.R., Kahle, A.B., Walker, R.E., 1986. Color enhancement of highly correlated images. I. Decorrelation and HSI contrast stretches. Remote Sensing of Environment 20, 209–235.

Gillespie, A., M atsunaga, A., R okugawa, S., H ook, S., 1998. Temperature and emissivity separation from Advanced Spaceborne Thermal Emission and Reflection Radiometer (ASTER) images. IEEE Transactions on Geoscience and Remote Sensing 36, 1113–1126.

Gushchenko, I.I., 1979. Eruptions of Volcanoes of the World: a Catalog. In: Academy of Science USSR Far Eastern Science Center. Nauka, Moscow, p. 474 (in Russian).

Heiken, G., Casadevall, T.J., Newhall, C., 1992. First international symposium on volcanic ash and aviation safety. Bulletin of Volcanology 54 (3), 250–251.

Hook, S., Dmochowski, J., Howard, K., Rowan, L., Karlstrom, K., Stock, J., 2005. Mapping weight percent silica variation from remotely acquired multispectral thermal infrared data with examples from the Hiller Mountains, Nevada, USA and Tres Virgenes-La Reforma, Baja California Sur, Mexico. Remote Sensing of Environment 95, 273–289.

Iwasaki, A., Tonooka, H., 2005. Validation of a crosstalk correction algorithm for ASTER/SWIR. IEEE Transactions on Geoscience and Remote Sensing 43 (12), 2747–2751.

Johnson, P.E., Smith, M.O., Adams, J.B., 1992. Simple algorithms for remote determination of mineral abundances and particle sizes from reflectance spectra. Journal of Geophysical Research 97, 2649–2657.

Kahle, A.B., Madura, D.P., Soha, J.M., 1980. Middle infrared multispectral aircraft scanner data: analysis for geological applications. Applied Optics 19, 2279–2290.

Kahle, A., Palluconi, F., Hook, S., Realmuto, V., Bothwell, G., 1991. The Advanced Spaceborne Thermal Emission and Reflectance Radiometer (ASTER). International Journal of Systematic Technology 3, 144–156.

Kamchatka Volcanic Eruption Response Team (KVERT) Report, 2005. Kliuchevskoi Volcano, 14 January through 13 May 2005. (http://www.avo.alaska.edu/activity/avoreport.php?view=kam info&id=&month=January&year=2005). Cited January 2007.

Kirianov, V.Y., Neal, C.A., Gordeev, E.I., Miller, T.P., 2002. KVERT (Kamchatkan Volcanic Eruptions Response Team): U.S. Geological Survey Fact Sheet. 064-02 (in English and Russian). Also online (http://geopubs.wr.usgs.gov/fact-sheet/fs064-02/).

Krasheninnikov, S.P., 1949. Description of Kamchatka Land. Moscow-Leningrad: Glavmorsevput, p. 841 (In Russian).

McAdoo, B.G., Richardson, N., Borreo, J., 2007. Inundation distances and run-up measurements from ASTER, QuickBird and SRTM data, Aceh coast, Indonesia. International Journal of Remote Sensing 28 (13–14), 2961–2975.

Miller, T.P., Casadevall, T.J., 2000. Volcanic ash hazards to aviation. In: Sigurdsson, H., Houghton, B., McNutt, S.R., Rymer, H., Stix, J. (Eds.), 2000. Encyclopedia of Volcanoes. Academic Press, San Diego, CA, pp. 915–930.

Miller, T.P., Kirianov, V.Y., Kelley, H.L., 1994. Klyuchevskoy Fact Sheet. U.S. Geological Survey Fact Sheet, vol. 94-067, p. 4. Also online (http://eq.giseis.alaska.edu/volcanoes/klyu/klyufact.html).

Morisette, J.T., Giglio, L., Csiszar, I., Justice, C.O., 2005. Validation of the MODIS active fire product over southern Africa with ASTER data. International Journal of Remote Sensing 26 (19), 4239–4264.

Ozerov, A., Ariskin, A., Kyle, P., Bogoyavlenskaya, G., Karpenko, S., 1997. Petrological–geochemical model for genetic relationships between basaltic and andesitic magmatism of Klyuchevskoi and Bezymiannyi Volcanoes, Kamchatka. Petrology 5 (6), 550–569.

Pieri, D.C., Abrams, M.J., 2004. ASTER watches the world's volcanoes: a new paradigm for volcanological observations from orbit. Journal of Volcanology and Geothermal Research 135, 13–28.

Pieri, D.C., Ma, C., Simpson, J.J., Hufford, G., Grindle, T., Grove, C., 2002. Analyses of in-situ airborne volcanic ash from the February 2000 eruption of Hekla Volcano, Iceland. Geophysical Research Letters 29 (16), 19.1–19.4.

Przedpelski, Z.J., Casadevall, T.J., 1994. Volcanic ash and aviation safety: Proceeding of the First International Symposium on Volcanic Ash and Aviation Safety. In: Casadevall, T.J. (Ed.), U.S. Geological Survey Bulletin, vol. 2047, pp. 129–136.

Ramsey, M.S., 2002. Ejecta distribution patterns at Meteor Crater, Arizona: on the applicability of lithologic end-member deconvolution for spaceborne thermal infrared data of Earth and Mars. Journal of Geophysical Research 107 (E8), 3.1–3.14.

Ramsey, M.S., Christensen, P.R., 1998. Mineral abundance determination: quantitative deconvolution of thermal emission spectra. Journal of Geophysical Research 103, 577–596.

Ramsey, M.S., Fink, J.H., 1999. Estimating silicic lava vesicularity with thermal remote sensing: a new technique for volcanic mapping and monitoring. Bulletin of Volcanology 61, 32–39.

Ramsey, M., Dehn, J., 2004. Spaceborne observations of the 2000 Bezymianny, Kamchatka eruption: the integration of high-resolution ASTER data into near real-time monitoring using AVHRR. Journal of Volcanology and Geothermal Research 135, 127–146.

Ramsey, M.S., Kuhn, S., 2004. Fusion of parametric and thematic data to characterize the Soufrière Hills volcanic dome. Abstract of the General Assembly, IAVCEI.

Ramsey, M.S., Rose, S.R., 2005. Field study of Kamchatkan volcanoes, Russia (Part II): Quantitative Investigation of Thermal Infrared (TIR) Heat Flux. UCIS Hewlett International Grant Program, University of Pittsburgh.

Ramsey, M.S., Dehn, J., Wessels, R., Byrnes, J., Duda, K., Maldonado, L., Dwyer, J., 2004. The ASTER emergency scheduling system: a new project linking near-real-time satellite monitoring of disasters to the acquisition of high-resolution remote sensing data. Fall Meeting Supplement, Abstract SF23A-0026: Eos Transactions AGU, vol. 85 (47).

Realmuto, V.J., 1990. Separating the effects of temperature and emissivity: Emissivity spectrum normalization. In: Abbott, E.A. (Ed.), Proceedings of the second Thermal Infrared Multispectral Scanner (TIMS) Workshop. Jet Propulsion Laboratory, Pasadena, CA.

Realmuto, V.J., Abrams, M.J., Buongiorno, M.F., 1994. The use of multispectral thermal infrared image data to estimate the sulfur dioxide flux from volcanoes: a case study from Mount Etna, Sicily, July 29, 1986. Journal of Geophysical Research 99 (B1), 481–488.

Realmuto, V.J., Sutton, A.J., Elias, T., 1997. Multispectral thermal infrared mapping of sulfur dioxide plumes: a case study from the East rift zone of Kilauea volcano, Hawaii. Journal of Geophysical Research 102 (B7), 15057–15072.

Ripepe, M., Harris, A.L., Carniel, R., 2002. Thermal, seismic and infrasonic evidences of variable degassing rates at Stromboli volcano. Journal of Volcanology and Geothermal Research 118, 285–297.

Roach, A.L., Benoit, J.P., Dean, K.G., McNutt, S.R., 2004. The combined use of satellite and seismic monitoring during the 1996 eruption of Pavlof volcano, Alaska. Bulletin of Volcanology 62 (6–7), 385–399.

Rothery, D., 1989. Volcano monitoring by satellite. Geology Today 5 (4), 128–132.

Sabol, D.E., Adams, J.B., Smith, M.O., 1992. Quantitative subpixel spectral detection of targets in multispectral images. Journal of Geophysical Research 97, 2659–2672.

Self, S., Walker, G.L., 1994. Volcanic ash and aviation safety: Proceeding of the First International Symposium on Volcanic Ash and Aviation Safety. In: Casadevall, T.J. (Ed.), U.S. Geological Survey Bulletin, vol. 2047, pp. 65–74.

Searcy, C.K., Dean, K., Stringer, B., 1998. PUFF: a volcanic ash tracking and prediction model. Journal of Volcanology and Geothermal Research 40, 1–16.

Smithsonian National Museum of Natural History Global Volcanism Program (Gvp), 2008. Kliuchevskoi Volcano Eruptive History. (http://www.volcano.si.edu/world/volcano.cfm?vnum=1000-26=&volpage=erupt).

Tralli, D.M., Blom, R.G., Zlotnicki, V., Donnellan, A., Evans, D.L., 2005. Satellite remote sensing of earthquake, volcano, flood, landslide and coastal inundation hazards. ISPRS Journal of Photogrammetry and Remote Sensing 59 (4), 185–198.

Urai, M., Fukui, K., Yamaguchi, Y., Pieri, D.C., 1999. Volcano observation potential and global volcano monitoring plan with ASTER. Bulletin of the Volcanological Society of Japan 44 (3), 131–141.

Vaughan, R.G., Hook, S.J., Ramsey, M.S., Realmuto, V.J., Schneider, D.J., 2005. Monitoring eruptive activity at Mount Saint Helens with TIR image data. Geophysical Research Letters 32, L10305.

Wooster, M.J., Kaneko, T., 2001. Testing the accuracy of solar-reflected radiation corrections applied during satellite shortwave infrared thermal analysis of active volcanoes. Journal of Geophysical Research 106 (B7), 13381–13393.

Yamaguchi, Y., Kahle, A., Tsu, H., Kawakami, T., Pniel, M., 1998. Overview of the Advanced Spaceborne Thermal Emission and Reflectance Radiometer (ASTER). IEEE Transactions on Geoscience and Remote Sensing 36, 1062–1071.

Zorn, N.V., Ramsey, M.S., 2002. An automated spectral deconvolution algorithm: application to thermal infrared studies of Earth and Mars. Solar System Remote Sensing, LPI Contribution, No. 1129, pp. 93–94.